

***Ab initio* Phase Diagram of Ta₂O₅**

Yan Gong^{1,2,#}, Huimin Tang^{3,#}, Yong Yang^{1,2,*}, and Yoshiyuki Kawazoe^{4,5}

¹*Key Lab of Photovoltaic and Energy Conservation Materials, Institute of Solid State Physics, HFIPS, Chinese Academy of Sciences, Hefei 230031, China*

²*Science Island Branch of Graduate School, University of Science and Technology of China, Hefei 230026, China*

³*College of Physics and Technology, Guangxi Normal University, Guilin 541004, China*

⁴*New Industry Creation Hatchery Center, Tohoku University, Sendai, 980-8579, Japan*

⁵*Center for Interdisciplinary Research, SRM University-AP, Neerukonda, Mangalagiri Mandal, Guntur District, Andhra Pradesh, 522240, India*

Tantalum pentoxide (Ta₂O₅) is a polymorphic wide-bandgap semiconductor with outstanding dielectric properties and widespread use in optical and electronic technologies. Its rich structural diversity, arising from multiple polymorphs accessible under different synthesis conditions, has made Ta₂O₅ a long-standing subject of interest. However, a unified understanding of the thermodynamic stability and phase transitions of its polymorphs across pressure-temperature (P-T) space has remained elusive. Here, using first-principles calculations, we map the thermodynamic landscape of Ta₂O₅ and establish a comprehensive P-T phase diagram together with a phase-stability hierarchy. We find that γ -Ta₂O₅ and B-Ta₂O₅ dominate the phase diagram over a broad range of P-T conditions: γ -Ta₂O₅ is stabilized at low pressures, while B-Ta₂O₅ becomes thermodynamically favored at higher pressures up to \sim 60 GPa, beyond which Y-Ta₂O₅ emerges as the most stable phase. Crucially, nuclear quantum effects (NQEs) are shown to play a significant role in determining relative phase stability, contributing substantially to the Gibbs free energy and altering phase boundaries. A re-entrant phase transition between γ - and B-Ta₂O₅ is predicted near \sim 2 GPa, revealing unexpected complexity in the phase behavior of this oxide. More generally, we identify a characteristic temperature (T₀), at which zero-point and thermal phonon contributions to the free energy become comparable, and show that T₀ is approximately one-third of the Debye temperature. This relationship provides a simple, physically transparent criterion for assessing the importance of NQEs in phase stability, with implications extending beyond Ta₂O₅ to a broad class of complex oxides.

*Corresponding Author: yyanglab@issp.ac.cn

These authors contribute equally to this work.

I. Introduction

Tantalum pentoxide (Ta_2O_5) is a versatile and critical material in modern science and engineering, due to its wide bandgap, high dielectric constant, and remarkable chemical stability. These properties have enabled its widespread application in optoelectronic devices [1-4], resistive random-access memory (RRAM) [5-10], and catalysis [11-13].

In optics, Ta_2O_5 is used as an anti-reflective coating in photovoltaic devices [14,15] and as a promising material for ultraviolet photodetectors [16,17]. In electronics, its high dielectric constant supports the miniaturization of capacitors [18,19] and dielectric materials [20,21]. Additionally, Ta_2O_5 is employed in catalysis for hydrogen production [22-24] and as a coating material in biomedical engineering to enhance biocompatibility and corrosion resistance [25-27]. These unique properties position Ta_2O_5 as a promising material for cutting-edge technologies in renewable energy and advanced medical devices.

A thorough understanding of Ta_2O_5 polymorphism is essential to fully harness its functional properties. Research in this area can be divided into two main avenues: experimental observation and theoretical understanding. In 1952, Lagergren and Magnéli reported a high-temperature Ta_2O_5 phase, providing one of the earliest experimental glimpses into the Ta-O system and laying the groundwork for subsequent structural investigations [28]. Throughout the 1960s, systematic powder X-ray diffraction (XRD) studies revealed multiple orthorhombic and hexagonal polymorphs, establishing a foundation for the rational exploration of Ta_2O_5 crystal chemistry [29,30]. Based on this experimental data, Stephenson and Roth proposed the L_{SR} model in 1971—an orthorhombic structural model containing 11 formula units (22 Ta/55 O)-though it required oxygen vacancies to maintain stoichiometry [31]. Researchers subsequently developed simplified versions of the L_{SR} model, including the β_{AL} model by Aleshina and Loginova [32] and the β_R model by Ramprasad [33]. High-pressure experiments discovered the B and Z phases [34], while thin-film deposition techniques such as chemical vapor deposition and magnetron sputtering successfully prepared the hexagonal δ -phase [35]. In 1992, Hummel *et al.* reported the

synthesis of TT-Ta₂O₅ and determined via X-ray diffraction its lattice parameters ($a = 3.639 \text{ \AA}$, $c = 3.901 \text{ \AA}$) and confirmed its P6/mmm space group, though the precise atomic structure remained unresolved [36]. By the 21st century, high-resolution synchrotron radiation and electron microscopy experiments had progressively refined the Ta₂O₅ polymorph database, providing reliable references for theoretical studies.

On the theoretical side, first-principles calculations and structure search algorithms played pivotal roles in elucidating the stability of Ta₂O₅ polymorphs. In 1997, Fukumoto and Miwa used density functional theory (DFT) to precisely resolve the atomic structure of the δ -phase [37] for the first time, confirming its P6/mmm space group and strong agreement with experimental diffraction patterns [36]. Later, Lee *et al.* proposed the orthorhombic λ -phase (Pbam space group) and demonstrated its lower energy (higher stability) than the L_{SR} model [38]. In 2016, Perez-Walton *et al.* systematically compared the thermodynamic and kinetic stabilities of multiple Ta₂O₅ phases, finding that those composed of TaO₆ octahedra (e.g., B, λ , β_{AL}) exhibited the lowest formation energies and dynamical stability, whereas structures incorporating higher-coordination polyhedra (e.g., TaO₇, TaO₈)-such as L_{SR}, L_G, T, H, δ , and Z-were either higher in energy or dynamically unstable, existing only under metastable or defective polymorphs [39]. In 2018, Yang and Kawazoe employed *ab initio* method and evolutionary algorithms to predict a new stable phase (γ -phase) [40] consisting entirely of ordered, distorted TaO₆ octahedral networks, establishing it as the most plausible ground-state theoretical model at low temperatures [41,42]. Further, in 2023, Yang's group combined particle swarm optimization (PSO) and DFT calculations to identify the stable triclinic γ_1 -Ta₂O₅ under ambient pressure, whose unit cell contains only one formula unit ($Z = 1$) [43].

While previous theoretical studies have focused on predicting the possible new individual Ta₂O₅ phases, a comprehensive understanding of their interrelationships (e.g., mutual transitions between every two phases) requires thermodynamic and/or kinetic analyses. Generally, the relationships among different crystal phases of a compound can be established through phase diagrams. The study of phase diagrams is crucial for revealing the dependence of material structures on temperature and

pressure, providing precise temperature-pressure (T-P) windows for experimental synthesis, and predicting material behavior under extreme conditions, thereby bridging theoretical predictions with practical applications. Brennan *et al.* systematically compared various proposed Ta_2O_5 structures using room-temperature high-pressure synchrotron XRD and DFT calculations, identifying seven potential phase models for the powder samples of Ta_2O_5 [44]. Their analysis revealed consistent equation-of-state parameters ($K_0 = 138 \pm 3.68$ GPa, $K'_0 = 1.82 \pm 0.45$.) across all candidate phases, and identified the λ -phase to be the best structural model for the Ta_2O_5 samples employed in their study. They also confirmed the pressure-induced amorphization of Ta_2O_5 at approximately 25 GPa, which shows remarkable consistency with the critical amorphization pressure reported in prior studies [45,46], thereby reinforcing the reproducibility of this phase transition behavior. To further resolve structural uncertainties, they conducted neutron diffraction experiments on Ta_2O_5 powders at temperatures up to 1000 °C [47]. The enhanced sensitivity of neutron diffraction to oxygen positions in the presence of heavy Ta atoms provided evidence that an orthorhombic L_{SR}-type structure best explains the experimental data, outperforming other theoretical models. In spite of these progresses, the lack of simultaneous high-pressure studies means a complete pressure-temperature (P-T) phase diagram remains unestablished [44,47]. Recently, we predicted a potential orthorhombic phase, termed Y- Ta_2O_5 , under high-pressure conditions using DFT calculations combined with structure-searching algorithms [48]. This phase contains four formula units per unit cell ($Z = 4$) and exhibits the highest known Ta–O coordination number among all reported Ta_2O_5 polymorphs. This study revealed that Y- Ta_2O_5 is the most energetically favorable phase of Ta_2O_5 within the pressure range of approximately above 60 GPa to at least 200 GPa [48]. Despite these advances, a complete phase diagram across wide temperature-pressure ranges remains lacking.

Building upon previous studies, this paper systematically evaluates the thermodynamic stability of various Ta_2O_5 polymorphs under a wide range of temperature and pressure conditions using first-principles calculations. A

comprehensive equilibrium phase diagram and a phase stability order diagram are established, offering a robust theoretical data for understanding phase transitions in Ta_2O_5 polymorphs.

Another focus is on the nuclear quantum effects (NQEs) [49-56]. It is shown that the phonon energy (E_{ph}), as a quantity due to NQEs, induces significant modifications to the phase diagram and phase stability sequence. This observation demonstrates that NQEs remain significant even in systems lacking of light elements (e.g., hydrogen, helium). Further analysis revealed that the zero-point energy (ZPE) equals to the excited vibration energy at a characteristic temperature T_0 , which is found to be approximately one-third of the Debye temperature.

The contents of this paper are organized as follows: After the Introduction part, Section II introduces the theoretical method employed in this study and the technical details of the DFT calculations. Section III presents the *ab initio* results of phase diagram and phase stability diagram of Ta_2O_5 polymorphs under a wide range of temperature—pressure conditions, and analyzes in general the physical consequences due to nuclear quantum effects (NQEs), in particular the role of zero-point energy (ZPE). The main conclusion is presented in Section IV.

II. Methods

The Vienna Ab Initio Simulation Package (VASP) based on DFT was employed for structural optimization and total energy calculations [57,58]. The Kohn-Sham equations were solved using a plane-wave basis set with an energy cutoff of 600 eV, and the projector-augmented wave (PAW) method was used to describe ion-electron interactions [59,60]. The Perdew-Burke-Ernzerhof (PBE) [61] type generalized gradient approximation (GGA) was used to describe the exchange-correlation interactions of electrons. The structures of the γ , γ_1 , B , λ , L_{SR} , δ , β_{AL} , β_R , Z and Y phases of Ta_2O_5 were optimized, and their total energies were calculated as a function of unit cell volume. The resulting data were fitted to the energy-volume equation of state (EOS) to determine the equilibrium geometry of each phase. The Gibbs free energy were calculated with the aid of the PHONOPY package [62,63], which

accounts for both static electronic and phonon vibrational contributions based on density functional perturbation theory (DFPT) [64-66]. By offering a reliable foundation for comparing phase stability under different temperature and pressure conditions, it facilitates the precise construction of P-T phase diagram. In case of structural relaxation and total energy calculations, the following k-point meshes generated using the Monkhorst-Pack scheme [67] were used for Brillouin zone (BZ) sampling of the indicated phase: $8 \times 8 \times 2$ for γ , $8 \times 8 \times 6$ for γ_1 , $2 \times 4 \times 4$ for B, $4 \times 4 \times 8$ for λ , $4 \times 2 \times 4$ for L_{SR} , $4 \times 4 \times 8$ for δ , $4 \times 8 \times 4$ for β_{AL} , $4 \times 4 \times 8$ for β_R , $4 \times 4 \times 4$ for Z, and $2 \times 4 \times 4$ for Y. In the DFPT calculations, the k-point meshes were uniformly reduced by a factor of two along each reciprocal lattice direction. Accordingly, $4 \times 4 \times 1$ for γ , $4 \times 4 \times 3$ for γ_1 , $1 \times 2 \times 2$ for B, $2 \times 2 \times 4$ for λ , δ , and β_R , $2 \times 1 \times 2$ for L_{SR} , $2 \times 4 \times 2$ for β_{AL} , $2 \times 2 \times 2$ for Z and $1 \times 2 \times 2$ for Y were used.

III. Results and Discussions

A. Constitutive Properties

The crystal unit cells of the ten phases of Ta_2O_5 (γ , γ_1 , B, L_{SR} , β_{AL} , λ , δ , β_R , Z, and Y) are schematically shown in Fig. 1. The crystal structure of Ta_2O_5 is primarily composed of TaO_n polyhedra, with Ta atoms at the centers and O atoms at the vertices [33,68,69]. Based on the number of oxygen atoms bonded to the central Ta atom, the polyhedra can be classified into four types: octahedron (TaO_6), pentagonal bipyramid (TaO_7), hexagonal bipyramid (TaO_8) and TaO_{10} polyhedra. Specifically, the β_{AL} , β_R , B, λ , γ , and γ_1 phases are composed of distorted octahedra; the hexagonal δ phase consists of edge-sharing octahedra and hexagonal bipyramids; the L_{SR} phase consists of corner-sharing octahedra and pentagonal bipyramids; the Z phase is composed solely of pentagonal bipyramids; and the Y phase consists of TaO_{10} polyhedra (Fig. 1). The optimized lattice parameters for the ten phases of Ta_2O_5 are presented in Table I. Notably, the Y phase only exists stably above 62 GPa, which can be viewed as the transformation of the B phase under such high-pressure condition.

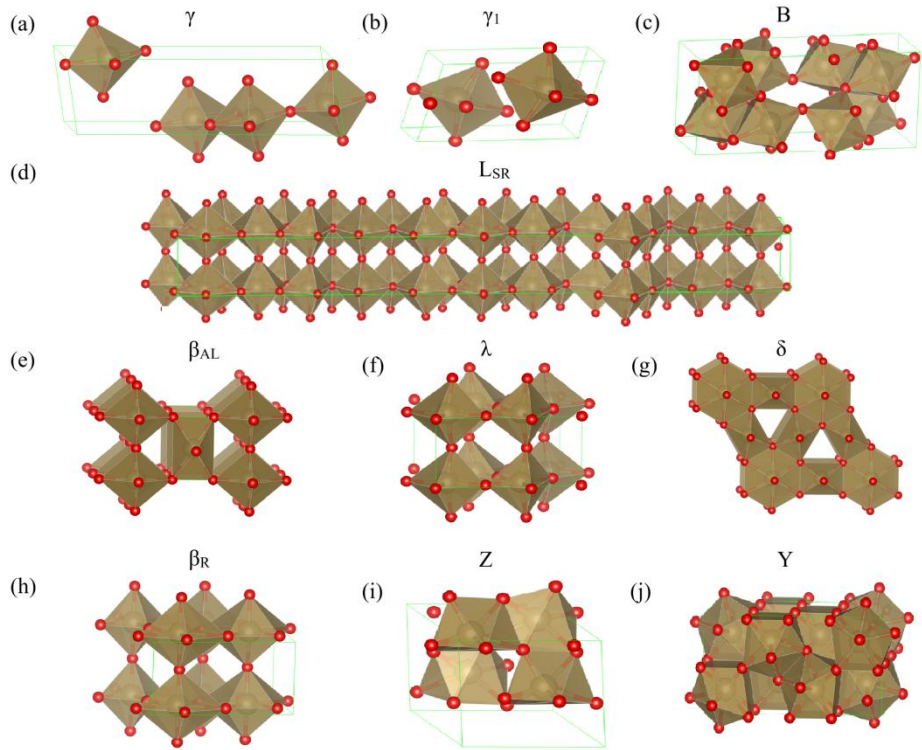


FIG. 1. Schematic diagram of the structure models of Ta_2O_5 : (a) γ ; (b) γ_1 ; (c) B; (d) L_{SR} ; (e) β_{AL} ; (f) λ ; (g) δ ; (h) β_R ; (i) Z and (j) Y. The O and Ta atoms are represented by smaller (red) and larger (brown) spheres, respectively.

Table I. The calculated lattice parameters of the ten Ta_2O_5 phases, where α , β , and γ represent the angles between the cell edges b and c , a and c , and a and b , respectively. Z represents the number of Ta_2O_5 formula units in the unit cell.

Ta_2O_5	a (Å)	b (Å)	c (Å)	α (°)	β (°)	γ (°)	Z
γ	3.89	3.89	13.38	81.77	98.25	89.98	2
γ_1	3.87	3.91	6.82	90.35	73.49	90.00	1
B	12.93	4.92	5.59	90.00	103.23	90.00	4
L_{SR}	6.33	40.92	3.85	90.00	90.00	89.16	11
β_{AL}	6.52	3.69	7.77	90.00	90.00	90.00	2
λ	6.25	7.40	3.82	90.00	90.00	90.00	2
δ	7.33	7.33	3.89	90.00	90.00	120.00	2

β_R	7.42	6.21	3.87	90.00	90.00	90.00	2
Z	6.05	5.19	5.82	90.00	118.33	90.00	2
Y	9.94	4.97	4.32	90.00	90.00	90.00	4

B. Phase Diagrams, Phase Stability Order Diagrams, and NQEs

In many-particle systems such as condensed phase materials, the Gibbs free energy is the fundamental thermodynamic quantity that dictates phase stability, phase transitions, and the construction of phase diagrams. For semiconductors and insulators, where electrons largely remain in their ground states at finite temperatures, the free energy is dominated by lattice contributions—namely, the internal lattice energy, the phonon free energy, and the pressure-volume term (PV). Under temperature T , pressure P and volume V , the Gibbs free energy (G) can be expressed as: $G = F + PV$, where $F = -k_B T \ln Z$, and $Z = \exp(-U/k_B T) \prod_j \frac{\exp(-\hbar\omega_j/2k_B T)}{[1 - \exp(-\hbar\omega_j/k_B T)]}$. It follows that:

$$F = U + \frac{1}{2} \sum_j \hbar\omega_j + k_B T \sum_j \ln[1 - \exp(-\hbar\omega_j/k_B T)] \quad (1)$$

where U represents the static free energy or zero-temperature ground state energy, which refers to the system's internal energy when phonons are not taken into account. Generally, it can be obtained directly through DFT calculations. k_B is the Boltzmann constant, and \hbar is the reduced Planck constant. The second term ($\frac{1}{2} \sum_j \hbar\omega_j$) is the zero-point energy (ZPE), which is due to the quantum motions of atoms (more precisely, the atomic nuclei) at absolute zero temperature ($T = 0$), and ω_j denotes the vibrational frequency of the j -th phonon mode. The phonon free energy $F_{ph}(V, T) = \frac{1}{2} \sum_j \hbar\omega_j + k_B T \sum_j \ln[1 - \exp(-\hbar\omega_j/k_B T)] = E_{ph} - TS$. The phonon energy $E_{ph} = \sum_j \left(\frac{1}{2} \hbar\omega_j + \frac{\hbar\omega_j}{e^{\hbar\omega_j/(k_B T)} - 1} \right)$, and the entropy term due to phonon is given by $TS = \sum_j \frac{\hbar\omega_j}{e^{\hbar\omega_j/(k_B T)} - 1} - k_B T \sum_j \ln[1 - \exp(-\hbar\omega_j/k_B T)]$.

These quantities can be readily obtained using VASP jointly with PHONOPY, which yields the Gibbs free energy $G(P, T) = U + F_{ph} + PV$. With the computed Gibbs free energies, the relative appearance probability of each polymorph can be

evaluated under given P - T conditions. The equilibrium phase diagram of Ta_2O_5 is constructed by comparing $G(P, T)$ across nine polymorphs (γ , γ_1 , B , λ , L_{SR} , δ , β_{AL} , β_{R} , and Z) over a range of pressures and temperatures, identifying the phase with the lowest G at each (P, T) point, as well as establishing the phase stability order diagram.

Figure 2 shows the temperature dependence of the Gibbs free energy, $G(T)$, for nine Ta_2O_5 polymorphs under pressures from 0 to 60 GPa, with the panels (a)-(h) representing 0, 6, 10, 20, 30, 40, 50, and 60 GPa, respectively. In all cases, the free energies decrease monotonically with temperature, reflecting the increasing contribution of vibrational entropy. At ambient pressure (panel a), the γ and γ_1 phases are the first two most stable, while the β_{AL} and Z phases are the least stable. As pressure rises, the relative free energies change significantly: the B phase becomes thermodynamically favored above 6 GPa, whereas the γ and γ_1 phases gradually lose their thermodynamical stability. Furthermore, the λ phase becomes the second most stable high-pressure phase when $P \geq 4.2$ GPa (inset of Fig. 2(b)), and remains so until ~ 31.8 GPa.

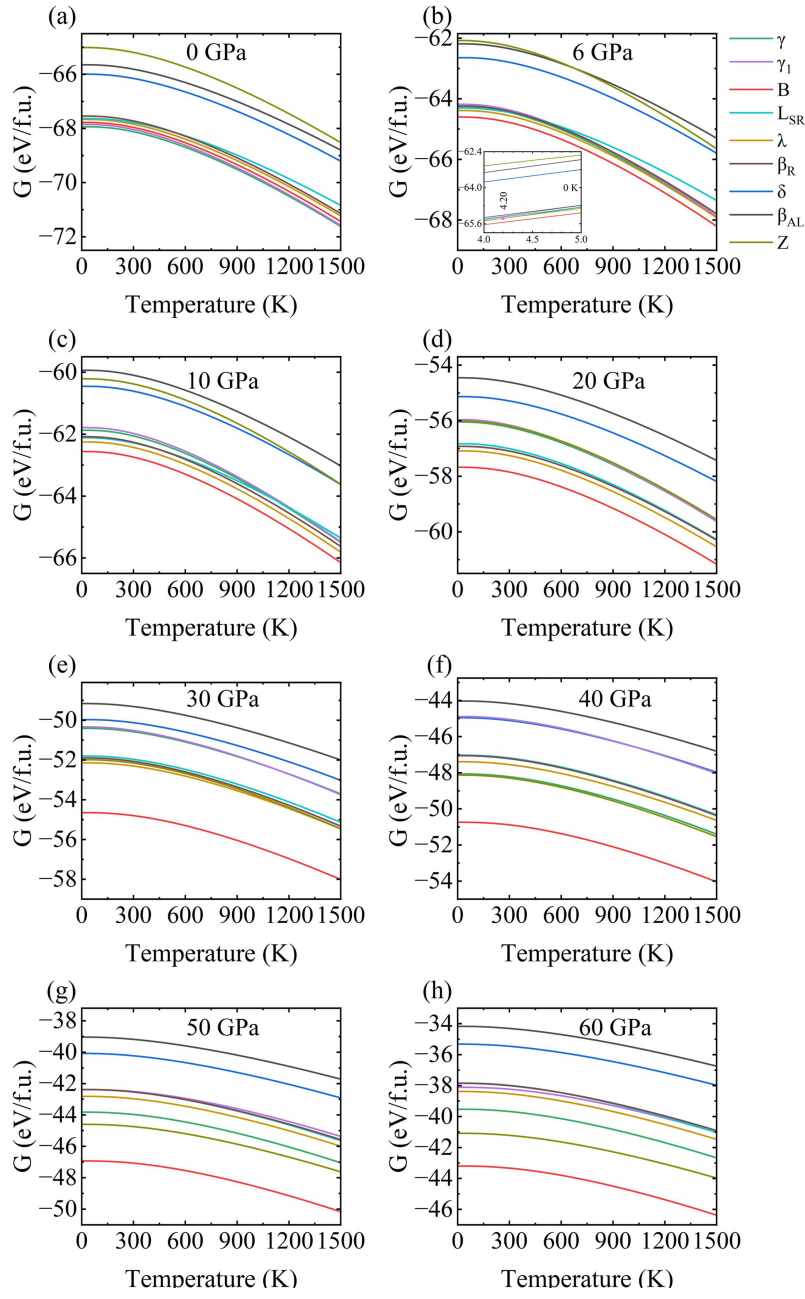


FIG. 2. Temperature-dependent Gibbs free energies $G(T)$ of nine Ta_2O_5 polymorphs under pressures from 0 to 60 GPa, in units of eV per formula unit (eV/f.u.). Panels (a)-(h) correspond to pressures of 0, 6, 10, 20, 30, 40, 50, and 60 GPa, respectively.

Table II provides an overview of the stability rankings of the nine Ta_2O_5 polymorphs over a broad pressure-temperature (P-T) range, covering temperatures of 0, 600, and 1200 K and pressures from 0 to 60 GPa. At $P \sim 0$ GPa (ambient pressure), the γ and γ_1 phases are the most and second-most stable, followed by the B and λ

phases, whereas the Z and β_{AL} phases exhibit the lowest stability. With increasing pressure, the stability hierarchy undergoes a pronounced restructuring: the B phase emerges as the most stable polymorph at intermediate and high pressures, while the relative stability of the γ - and γ_1 -type structures progressively decreases.

As further evidenced in Table II, the influence of temperature on the relative stability sequence is strongly pressure dependent. At $P = 0$ GPa, when the temperature increases to $T \geq 600$ K, only the stability order of L_{SR} and β_R is reversed, while the ordering of all other phases remains unchanged, and this sequence persists up to 1200 K. At $P = 20$ GPa, the temperature effect is similarly weak, with a stability reversal occurring only between Z and γ_1 at $T \geq 600$ K, and no further changes observed at 1200 K. At $P = 40$ GPa, the stability sequence remains identical from 0 to 600 K, whereas at 1200 K a minor reordering is observed exclusively between γ_1 and δ . At $P = 60$ GPa, the temperature effect is similarly weak, with a stability reversal occurring only between L_{SR} and β_R at $T \geq 600$ K, and no further changes observed at 1200 K. Together, these data in Table II illustrate how pressure and temperature change the stability hierarchy of Ta_2O_5 polymorphs.

Table II. The order of stability of Ta_2O_5 phases at a number of (P, T) points, with the pressure $P = 0, 20, 40, 60$ GPa, and temperature $T = 0, 600, 1200$ K.

(P, T)	Order of Stability								
	1	2	3	4	5	6	7	8	9
(0,0)	γ	γ_1	B	λ	L_{SR}	β_R	δ	β_{AL}	Z
(20,0)	B	λ	β_R	L_{SR}	γ	Z	γ_1	δ	β_{AL}
(40,0)	B	Z	γ	λ	β_R	L_{SR}	δ	γ_1	β_{AL}
(60,0)	B	Z	γ	λ	γ_1	β_R	L_{SR}	δ	β_{AL}
(0,600)	γ	γ_1	B	λ	β_R	L_{SR}	δ	β_{AL}	Z
(20,600)	B	λ	β_R	L_{SR}	γ	γ_1	Z	δ	β_{AL}
(40,600)	B	Z	γ	λ	β_R	L_{SR}	δ	γ_1	β_{AL}
(60,600)	B	Z	γ	λ	γ_1	L_{SR}	β_R	δ	β_{AL}

(0,1200)	γ	γ_1	B	λ	β_R	L_{SR}	δ	β_{AL}	Z
(20,1200)	B	λ	β_R	L_{SR}	γ	γ_1	Z	δ	β_{AL}
(40,1200)	B	Z	γ	λ	β_R	L_{SR}	γ_1	δ	β_{AL}
(60,1200)	B	Z	γ	λ	γ_1	L_{SR}	β_R	δ	β_{AL}

To describe the relative appearance probability of each Ta_2O_5 phase, we introduce the quantity $Z_0 = \sum_{i=1}^9 e^{-\Delta G_i/(k_B T)}$, which is similar to the partition function defined in statistical mechanics. Here, ΔG_i represents the free energy difference of the i th phase relative to the minimum of $G(P, T)$. The appearance probability of the i th phase is therefore evaluated as follows:

$$\Gamma_i(T, P) = \frac{e^{-\Delta G_i/(k_B T)}}{Z_0} \quad (2)$$

As shown in Fig. 3, the curves illustrate the thermodynamic probabilities of various Ta_2O_5 phases under a series of pressures as a function of temperature. Under zero or ambient pressure conditions, the γ phase dominates over a wide temperature range of 0-1300 K, followed by the γ_1 phase. As temperature increases, the thermodynamic probabilities clearly separate the phases into two distinct groups: The first group consists of six phases (γ , γ_1 , B, λ , L_{SR} , and β_R), while the second comprises three phases (δ , β_{AL} , and Z). Within each group, the occurrence probabilities of the phases tend to converge to the same value in the high-temperature region.

With increasing external pressure, the B phase rapidly becomes the most thermodynamically stable polymorph, while the stability hierarchy of metastable phases undergoes significant reorganization, splitting them into distinct groups (Figs. 3(b)-(d)). All metastable phases exhibit the same trend: their occurrence probabilities increase substantially with rising temperature. However, under a given external pressure, the relative stability ranking of phases remains essentially unchanged. This indicates that pressure exerts a more pronounced influence on Gibbs free energy than temperature within the range of pressure-temperature investigated. Fundamentally, 1 GPa pressure change induces an energy shift of ~ 6.25 meV per 1 \AA^3 volume change,

which is equivalent to a temperature variation of approximately 72.5 K, which explains the sluggish temperature-dependence of phase stability with comparison to pressure. This also helps to understand the variation trend of phase stability order presented in Table II.

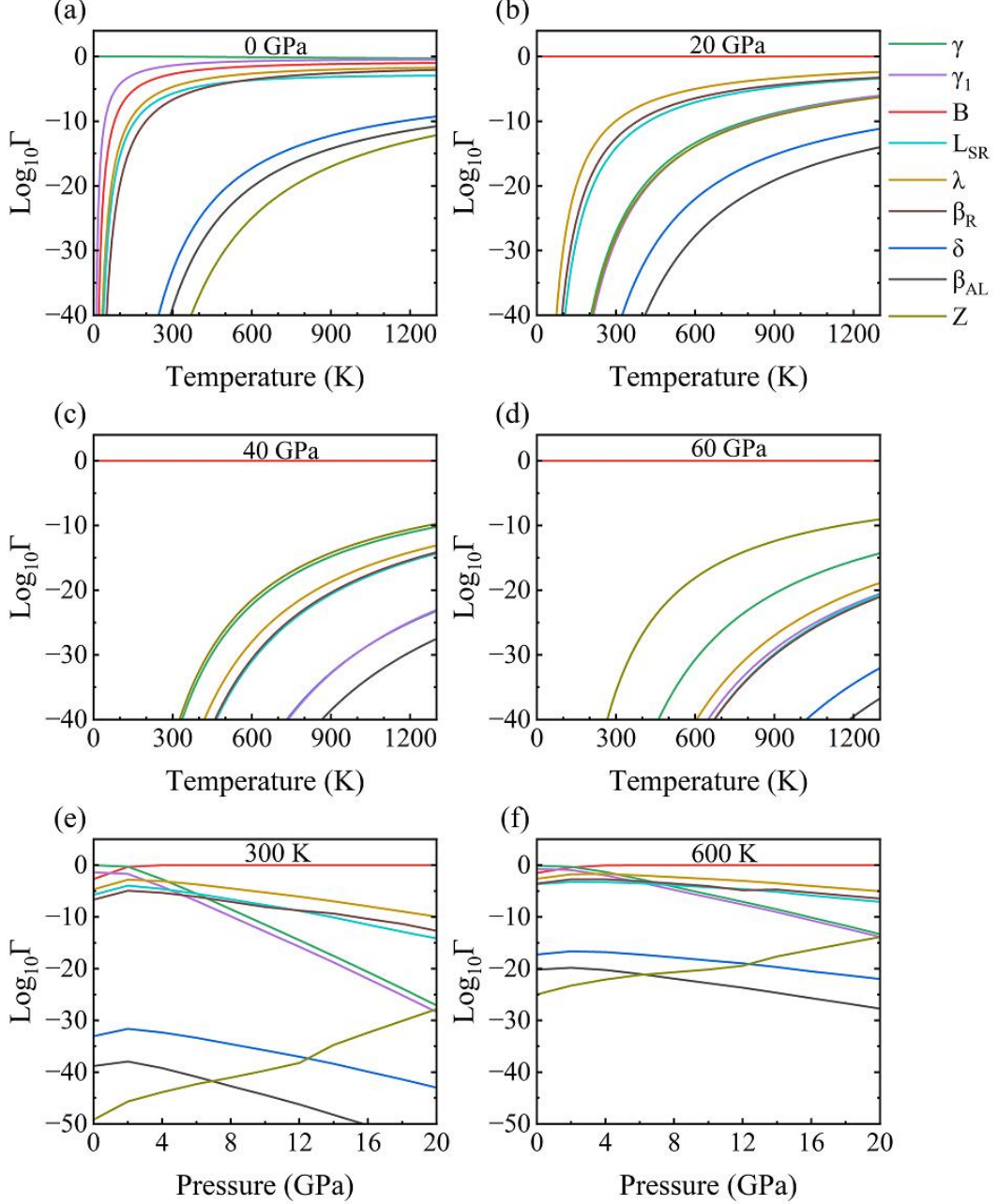


FIG. 3. Panels (a) to (d): Variation of the probability of occurrence of phase 9 under different pressure conditions, with pressure ranging from 0 GPa to 60 GPa in steps of 20 GPa. Panels (e)-(f): Probability of occurrence of phase at $T = 300, 600$ K, as a function of pressure.

Based on the analysis above, the Gibbs free energies of nine Ta_2O_5 polymorphs over a wide pressure-temperature (P-T) range were calculated to construct the equilibrium phase diagram. At each (P, T) point, the stable phase was identified as that with the lowest Gibbs free energy (Fig. 4). By including phonon contributions, we can assess the effects of nuclear quantum motions (i.e., the NQEs) on phase stability and transition boundaries, in comparison to the results of neglecting NQEs. As seen from Fig. 4(a), when phonon contributions are included, the $\gamma \rightarrow \text{B}$ phase transition occurs at ~ 2.0 GPa and 60 K, and the reverse transition ($\text{B} \rightarrow \gamma$) at ~ 2.0 GPa and 208 K. In contrast, under the static lattice approximation [Fig. 4(b)], the $\text{B} \rightarrow \gamma$ transition shifts dramatically to higher temperatures, occurring at $P = 2.0$ GPa and $T = 571$ K. Similarly, the $\text{Y} \rightarrow \text{B}$ transition boundary shifts from the (P, T) point of $\sim (62$ GPa, 50 K) to $\sim (62$ GPa, 370 K). These results reveal that NQEs can dramatically change the phase transition temperatures, reshaping the Ta_2O_5 phase diagram.

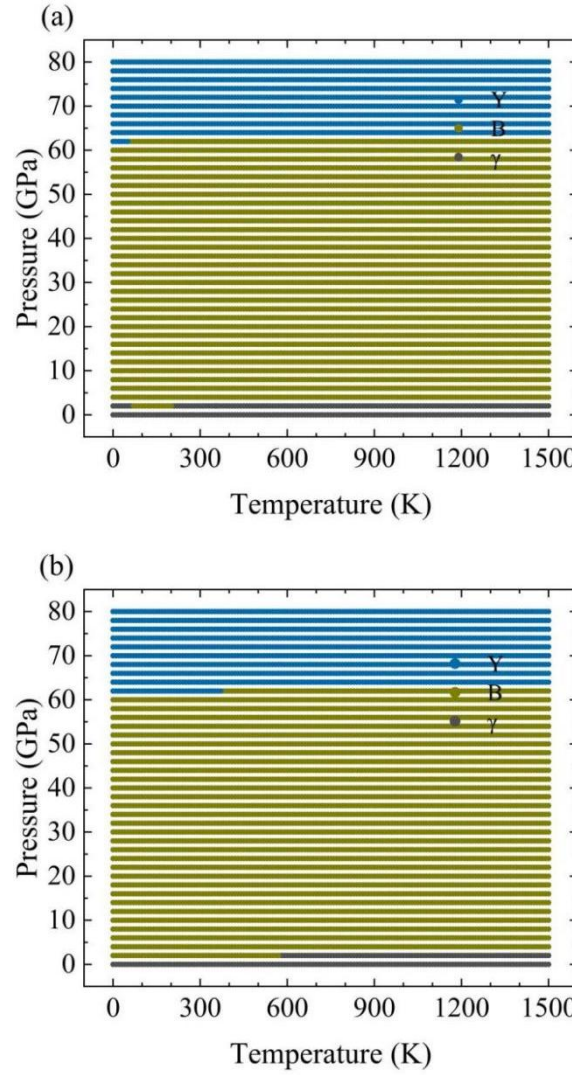


FIG. 4. (a) Phase diagram of Ta₂O₅ under different temperature and pressure conditions. (b) Temperature–pressure phase diagram of Ta₂O₅ within the static lattice approximation (neglecting phonon contributions).

Table III further illustrates how the inclusion of phonon free-energy contributions (E_{ph}) affects the stability ordering of the nine Ta₂O₅ polymorphs at $P \sim 0$ GPa (ambient pressure). The results show that incorporating E_{ph} leads to noticeable modifications in the relative stability, particularly at elevated temperatures (e.g., 1500 K), where phonon contributions induce a reordering of the terminal phases of the stability order sequence (β_{AL} and Z). This demonstrates that the phonon-derived free-energy term plays a substantive role in reshaping the phase sequence, especially

when thermal vibrations become significant. Overall, while the major phases— γ , γ_1 , B , and λ —maintain a consistent order across the examined temperature range, the inclusion of E_{ph} clearly alters the relative stability among several metastable phases, highlighting that phonon contributions constitute an essential factor governing the ambient-pressure phase-stability landscape of Ta_2O_5 .

Table III. Temperature-dependence of the order of stability of nine Ta_2O_5 polymorphs at pressure $P = 0$.

Temperature (K)	Order of Stability
0 (without E_{ph})	$\gamma > \gamma_1 > B > \lambda > L_{SR} > \beta_R > \delta > \beta_{AL} > Z$
0 (with E_{ph})	$\gamma > \gamma_1 > B > \lambda > L_{SR} > \beta_R > \delta > \beta_{AL} > Z$
300 (without E_{ph})	$\gamma > \gamma_1 > B > \lambda > L_{SR} > \beta_R > \delta > \beta_{AL} > Z$
300 (with E_{ph})	$\gamma > \gamma_1 > B > \lambda > L_{SR} > \beta_R > \delta > \beta_{AL} > Z$
600 (without E_{ph})	$\gamma > \gamma_1 > B > \lambda > \beta_R > L_{SR} > \delta > \beta_{AL} > Z$
600 (with E_{ph})	$\gamma > \gamma_1 > B > \lambda > \beta_R > L_{SR} > \delta > \beta_{AL} > Z$
900 (without E_{ph})	$\gamma > \gamma_1 > B > \lambda > \beta_R > L_{SR} > \delta > \beta_{AL} > Z$
900 (with E_{ph})	$\gamma > \gamma_1 > B > \lambda > \beta_R > L_{SR} > \delta > \beta_{AL} > Z$
1200 (without E_{ph})	$\gamma > \gamma_1 > B > \lambda > \beta_R > L_{SR} > \delta > \beta_{AL} > Z$
1200 (with E_{ph})	$\gamma > \gamma_1 > B > \lambda > \beta_R > L_{SR} > \delta > \beta_{AL} > Z$
1500 (without E_{ph})	$\gamma > \gamma_1 > B > \lambda > \beta_R > L_{SR} > \delta > Z > \beta_{AL}$
1500 (with E_{ph})	$\gamma > \gamma_1 > B > \lambda > \beta_R > L_{SR} > \delta > \beta_{AL} > Z$

Then we extended the datasets in Tables II and III, systematically analyzing the thermodynamic stability sequence of different Ta_2O_5 polymorphs under a set of temperature-pressure conditions. Using a pressure and temperature increment of $\Delta P = 2$ GPa and $\Delta T = 100$ K, Fig. 5 quantifies phase stability evolution across a broad temperature-pressure conditions, directly comparing the cases with/without phonon contributions. The phase stability order at a given P-T condition is then determined. For instance, at ambient pressure (0 GPa, 0 K), the stability sequence follows $\gamma > \gamma_1 > B > \lambda > L_{SR} > \beta_R > \delta > \beta_{AL} > Z$. A comparison between Fig. 5(a) and Fig. 5(b) reveals that the stability sequence is significantly altered, underscoring the critical role of phonon contributions and NQEs in refining the phase boundaries and stability

hierarchy.

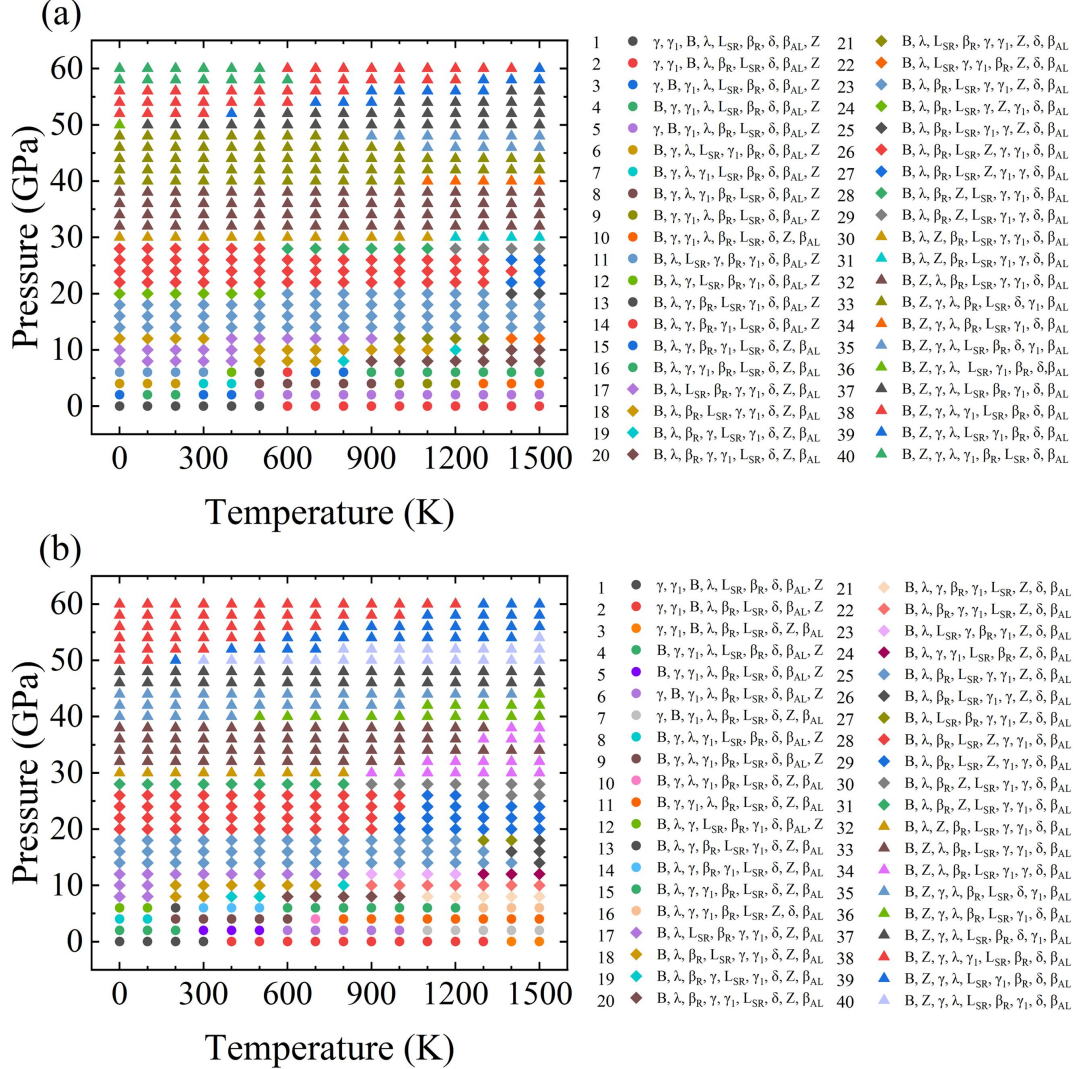


FIG. 5. (a) Stability sequence of each phase at a pressure variation step of $\Delta P = 2$ GPa and a temperature step of $\Delta T = 100$ K. (b) Stability sequence of various Ta_2O_5 polymorphs calculated with a pressure step of 2 GPa and a temperature step of 100 K, under the static lattice approximation (excluding phonon contributions).

To further refine the analysis, we conducted detailed calculations in the vicinity of the first intersection point in the phase diagrams for both scenarios with and without phonon contributions. This allows us to accurately determine the phase transition pressures (P_c) and temperatures (T_c). As shown in Fig. 6(a), when phonon

energy contributions are taken into account, the $\gamma \rightarrow B$ transition of Ta_2O_5 occurs at $P_c = 2.0$ GPa and $T_c = 60$ K. Upon further heating, the B phase at the same pressure reversely transforms back to the γ phase at approximately 208 K. Such a non-monotonic stability sequence—“stable phase \rightarrow metastable phase \rightarrow stable phase” under fixed pressure—is a hallmark of re-entrant phase transition behavior. Re-entrant transitions have been observed or predicted in some materials, including the triangular antiferromagnetic re-entrance in the antiperovskite Mn_3ZnN [70], the $\alpha \rightarrow \gamma \rightarrow \alpha$ non-monotonic sequence in solid nitrogen at ultralow temperatures and high pressures [71], the II \rightarrow III \rightarrow II re-entrant structural progression of CF_4 under compression [72], the metal–semiconductor–metal electronic re-entrance in lithium [73], as well as symmetry-cycling transitions such as SmC–SmA–SmC in various molecular crystals and liquid-crystal systems driven by enthalpy–entropy competition [74,75]. To our knowledge, this work is the first report on the re-entrant transition in transition metal oxide. In contrast, Fig. 6(b) presents the results without phonon contributions, where the γ -to-B phase transition takes place under single P-T points: 1.8 GPa at 167 K, 1.9 GPa at 340 K, and 2.0 GPa at 571 K. The re-entrant transition is clearly absent, which demonstrates again the significant role of NQEs in modifying the phase diagram. Collectively, these studies reveal a common observation: under constant pressure or external fields, the free energy of a system does not necessarily vary monotonically with temperature, but may reverse multiple times due to changes in vibrational entropy, magnetic entropy, volume effects, or molecular rearrangements, thereby giving rise to re-entrant phase transitions.

Against this backdrop, we performed high-precision quasiharmonic free-energy calculations for high-pressure phases of Ta_2O_5 . The results show that at $P = 2$ GPa (Fig. 6), the entropy and free-energy difference $G_B(T) - G_\gamma(T)$ exhibits a pronounced non-monotonic temperature dependence (see Figs. 6(c), 6(d)). At around 60 K, the free energies of the two phases intersect for the first time, making the γ phase thermodynamically more stable. As the temperature increases further, competition involving vibrational entropy again alters the free-energy ordering, leading to a second crossing near 208 K, where the B phase regains stability—constituting a

typical re-entrant sequence.

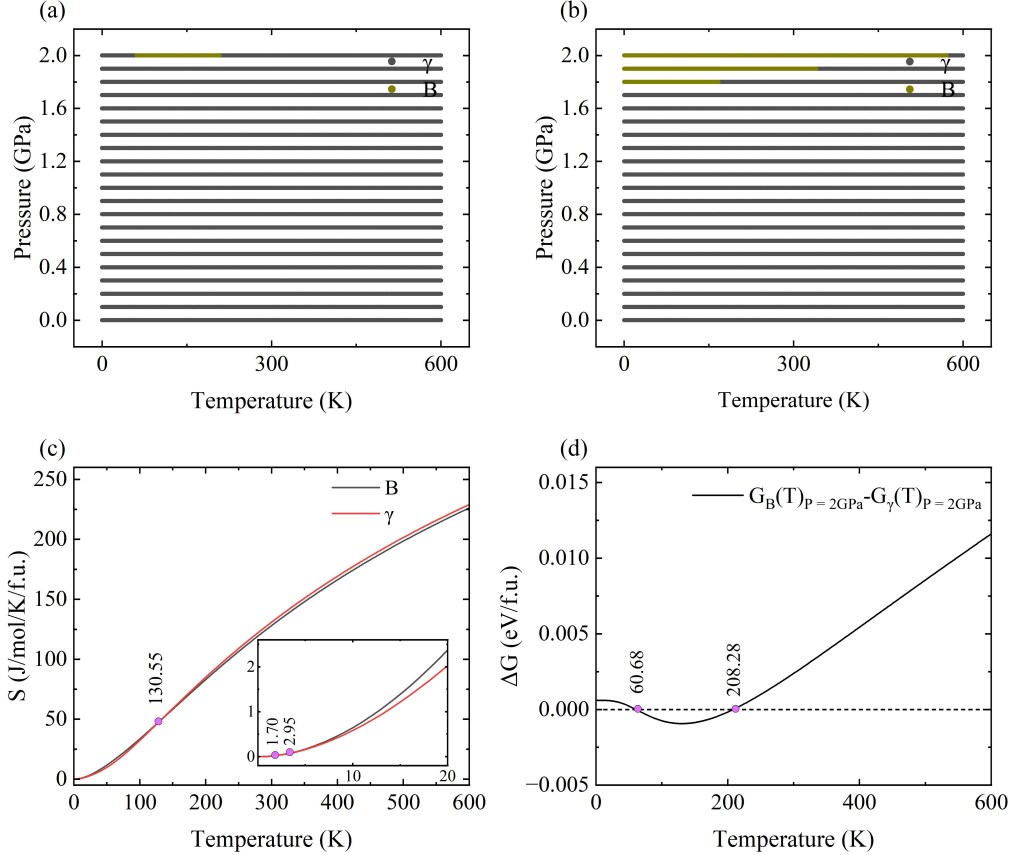


FIG. 6. The phase diagram of γ and B- Ta_2O_5 , calculated at a pressure step of 0.1 GPa and temperature step of 1 K, for the case with (panel a) and without (panel b) phonon energies. Temperature dependence of entropy (panbel c) and free energy difference (panel d) of γ and B- Ta_2O_5 .

C. The Zero-Temperature Phase Transition Pressure

At absolute zero ($T = 0$ K), the enthalpy of each phase is calculated as $H = E + PV$. A pressure-induced structural phase transition occurs when the enthalpies of two phases equal, with the corresponding pressure defined as the critical pressure (P_c).

$$P_c = (E_{\text{tot}2} - E_{\text{tot}1})/(V_1 - V_2) = -\Delta E/\Delta V, \quad (3)$$

where $E_{\text{tot}1}$ and $E_{\text{tot}2}$ represent the internal energies of two crystal structures, while V_1 and V_2 correspond to the volumes of these respective structures. Two situations were considered: (i) without zero-point energy (ZPE) correction, where $E_{\text{tot}} = E_0$, where E_0 is the ground-state energy; (ii) with ZPE correction, where $E_{\text{tot}} = E_0 +$

ZPE. The resulting critical pressures (P_{c1} (GPa) and P_{c2} (GPa, respectively) are summarized in Table IV. The discrepancies between P_{c1} and P_{c2} demonstrate that ZPE exerts a non-negligible effect on phase transition pressures near criticality.

For example, the $\gamma \rightarrow B$ transition pressure increases from 1.78 GPa (without ZPE) to 2.56 GPa (with ZPE), while the $\gamma_1 \rightarrow B$ transition shifts from 0.67 GPa to 1.48 GPa. These results demonstrate that incorporating the zero-point energy correction leads to nontrivial changes in the transition pressures, underscoring the importance of NQEs in accurately describing Ta_2O_5 phase stability.

Understanding the critical pressures at 0 K is essential for revealing how materials behave under extreme conditions. For Ta_2O_5 , the γ phases are more favorable at low pressures, while the B phase becomes increasingly stable at high pressures. The $\gamma \rightarrow B$ and $\gamma_1 \rightarrow B$ transition pressures further indicate that γ phases are more suitable for applications requiring stability at low pressures, whereas the B phase exhibits enhanced stability at high pressures. Furthermore, it can be seen from Table V that the disparity between P_{c1} and P_{c2} , ΔP ($= P_{c2} - P_{c1}$), for the transition from γ and γ_1 to the other polymorphs (e.g., B , λ , L_{SR} , ...) is very similar. This is due to the fact that the ground state energy and crystal volume per formula unit (mass density) of γ and γ_1 - Ta_2O_5 is very similar [43].

Table IV. Summary of critical pressures for various Ta_2O_5 phases, with $\Delta P = P_{c2} - P_{c1}$.

Ta_2O_5	γ, B	γ, λ	γ, L_{SR}	γ, β_R	γ, Z	β_R, Z	λ, Z	L_{SR}, Z
P_{c1} (GPa)	1.78	4.09	6.25	6.68	19.84	28.61	31.37	27.61
P_{c2} (GPa)	2.56	4.76	6.20	6.59	20.43	29.06	31.72	28.08
ΔP (GPa)	0.78	0.67	-0.05	-0.09	0.59	0.45	0.35	0.47
Ta_2O_5	γ_1, B	γ_1, λ	γ_1, L_{SR}	γ_1, β_R	γ_1, Z	β_{AL}, Z	δ, Z	γ_1, δ
P_{c1} (GPa)	0.67	2.74	4.61	5.21	19.34	6.09	11.73	39.16
P_{c2} (GPa)	1.48	3.37	4.47	5.15	19.94	7.42	12.53	38.99
ΔP (GPa)	0.81	0.63	-0.14	-0.06	0.60	1.33	0.80	-0.17

D. Role of Zero-Point Energy (ZPE) at Finite Temperatures

The analysis above comparing systems with and without phonon energy contributions quantitatively demonstrated that nuclear quantum effects (NQEs) significantly modify phase boundaries and stability sequences. We now systematically examine how zero-point energy (ZPE) contributes to crystal phonon energetics and its critical role in lattice dynamics and thermodynamic stability.

The phonon energy at a finite temperature T reads:

$$\begin{aligned} E_{ph} &= \sum_j \left(\frac{1}{2} \hbar \omega_j + \frac{\hbar \omega_j}{e^{\hbar \omega_j / (k_B T)} - 1} \right) = \sum_j \left(\frac{1}{2} \hbar \omega_j \right) + \sum_j \left(\frac{\hbar \omega_j}{e^{\hbar \omega_j / (k_B T)} - 1} \right) \\ &= ZPE + E_{ph,T>0} \end{aligned} \quad (4)$$

Aside from the ZPE term, the phonon energy at non-zero temperature ($E_{ph,T>0}$) may be expressed as follows:

$$E_{ph,T>0} = \sum_j \left(\frac{\hbar \omega_j}{e^{\hbar \omega_j / (k_B T)} - 1} \right) = \int_0^{\omega_m} \left[\frac{\hbar \omega}{e^{\hbar \omega / (k_B T)} - 1} \right] g(\omega) d\omega, \quad (5)$$

where ω_m denotes the maximum frequency and $g(\omega)$ is the vibrational density of states. Using Eq. (5), we can calculate the energy at non-zero temperature $E_{ph,T>0}$, then derive the total phonon energy E_{ph} using Eq. (4). The ZPE term and $g(\omega)$ were readily obtained using DFPT calculations. We further determined its relative contribution to the total phonon energy (Fig. 7). The results show that ZPE constitutes the major component at cryogenic temperatures and its proportion progressively drops with increasing T , consistent with the growing dominance of thermally activated lattice vibrations. Moreover, for a given temperature, the ZPE fraction increases systematically with pressure, indicating that compression enhances NQEs.

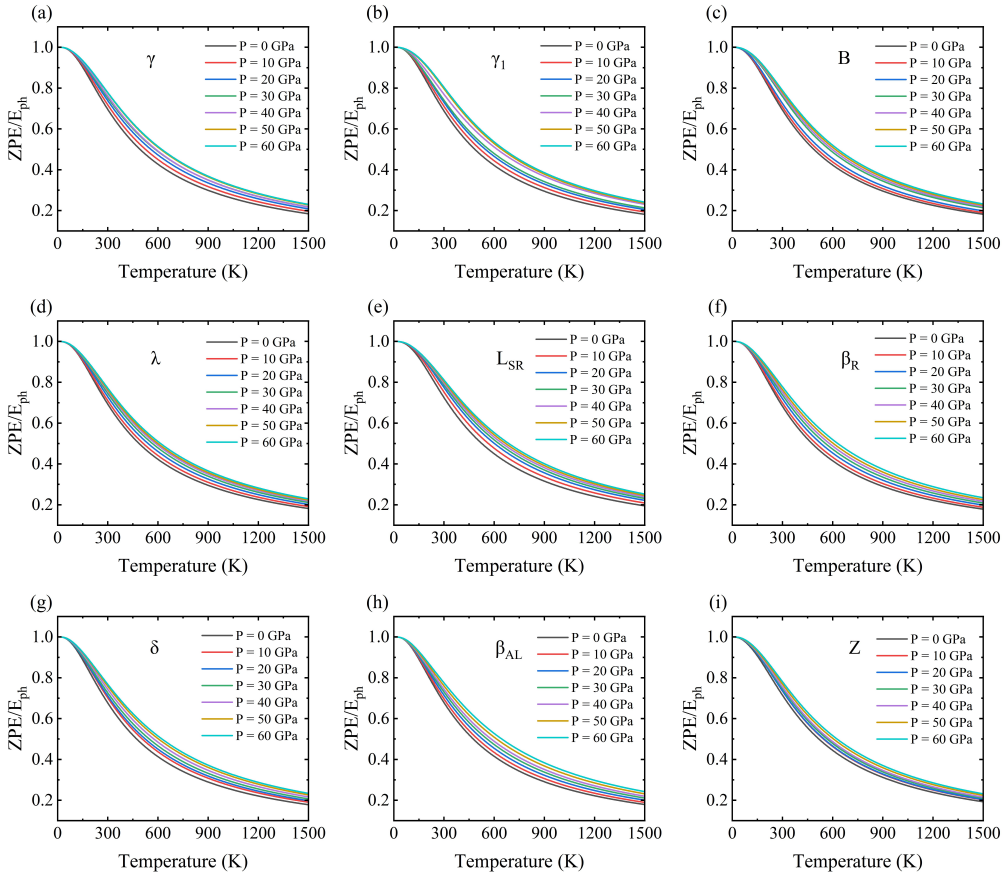


FIG. 7. Temperature dependence of the zero-point energy (ZPE) contribution to the total phonon energy E_{ph} of nine Ta_2O_5 polymorphs at different pressures.

We further investigated the role of ZPE in lattice dynamics by analyzing the ratio between zero-point energy (ZPE) and nonzero-temperature phonon energy $E_{\text{ph},T>0}$, identifying a characteristic temperature T_0 where their contributions become equal (i.e., $ZPE/E_{\text{ph},T>0} = 1$). As shown in Fig. 8, ZPE dominates the vibrational spectrum at cryogenic temperatures. Its role gradually decreases with increasing temperature and reaches the critical point T_0 , at which the zero-point and thermal motions of atoms contribute equally to the total phonon energies. The precisely determined T_0 serves as a fundamental parameter that quantifies the temperature range where quantum effects govern lattice behavior. These results establish T_0 as both a crucial metric for evaluating computational methods and a practical design parameter for quantum material applications. Concurrently, it can be seen that the contribution of ZPE

increases with pressure at a given temperature

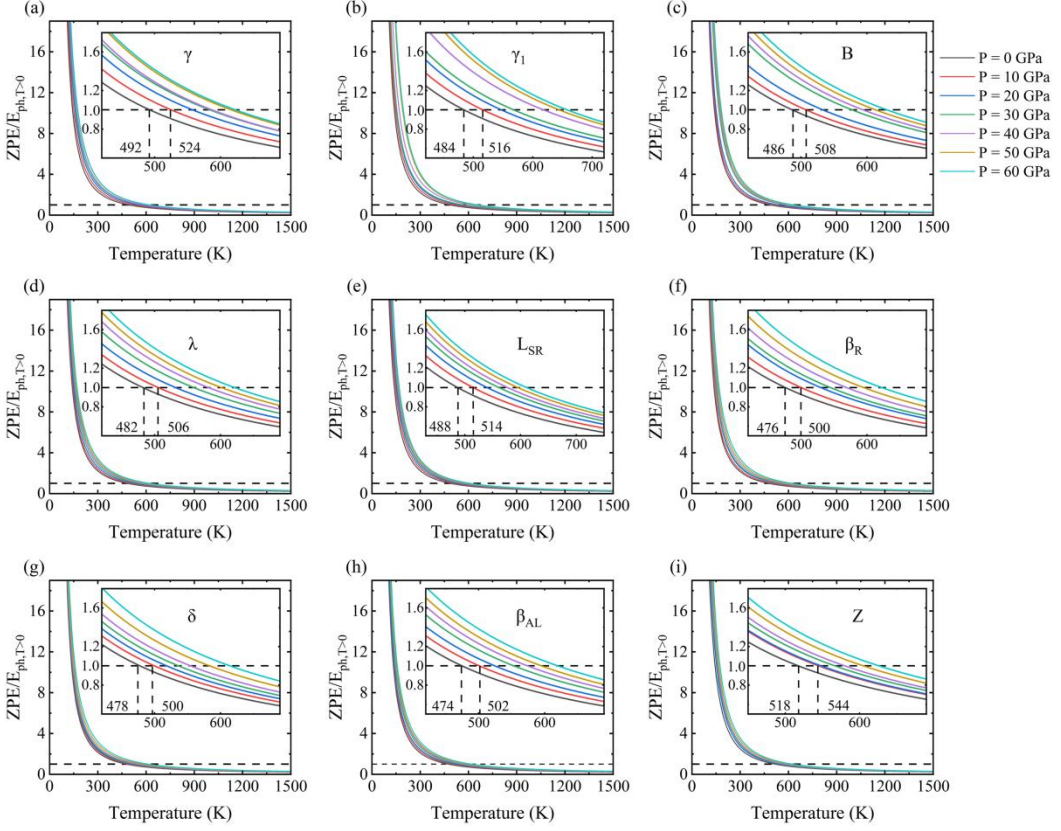


FIG. 8. Temperature dependence of the ratio between zero-point energy (ZPE) and nonzero-temperature phonon energy ($E_{ph,T>0}$) of nine Ta_2O_5 polymorphs at different pressures. The characteristic temperatures T_0 (where $ZPE/E_{ph,T>0} = 1$) are explicitly indicated (horizontal dashed lines).

Figure 9(a) presents the pressure dependence of the characteristic temperatures T_0 and their average of the nine Ta_2O_5 phases. Despite some fluctuations, the overall trend that pressure enhances T_0 and the role of ZPE in a given system is found. As shown by two of the authors [76], there exists a characteristic temperature ($\sim 1/3$ of the Debye temperature T_D) at which the atomic mean square displacement (MSD) due to zero-point and thermal motions are equal. To correlate these observations, we have further derived the maximum phonon frequency (ν_{max}) for each polymorph from DFPT calculations and estimated the corresponding Debye temperature ($T_D \sim h\nu_{max}/k_B$), where h is the Planck constant and k_B the Boltzmann constant. Shown in Fig. 9(b), are the calculated T_D/T_0 values for the nine Ta_2O_5 polymorphs with varying

pressures. Within a broad range of pressure, the number T_D/T_0 is nearly constant for each polymorph, which is roughly described by $T_D/T_0 = \mu \sim (3 \pm 0.5)$. In particular, four phases (γ , γ_1 , δ , β_R) exhibit excellent agreement with the relation of $T_D/T_0 = 3$, with discrepancies smaller than 3%. This coincidence implies that the Debye model accounts for the phonon properties of these Ta_2O_5 phases (γ , γ_1 , δ , β_R). Considering the fact that the vibrational frequency is proportional to the inverse of MSD [76] (equivalently, the phonon energy), the characteristic temperature which yields equal MSDs would give approximately the same energies for both zero-point and thermal phonons. These results provide preliminary support for extension of the earlier theoretical prediction regarding the relationship between the Debye temperature and the quantum-to-thermal crossover point [76], from elemental crystal systems to much more complex transition metal oxides.

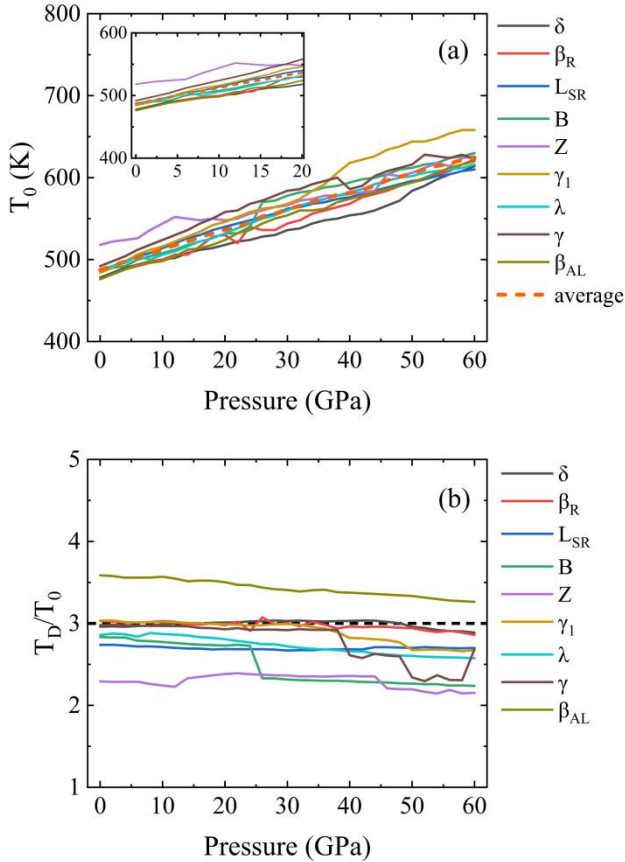


FIG. 9. Pressure dependence of the characteristic temperature T_0 (panel a) and its ratio to the Debye temperature (T_D/T_0 , panel b), for the Ta_2O_5 polymorphs studied above.

IV. Conclusions

In summary, this study establishes a comprehensive phase diagram of Ta_2O_5 across a broad temperature and pressure range using first-principles calculations. The γ - Ta_2O_5 and B - Ta_2O_5 are identified as two primary stable phases, with γ - Ta_2O_5 dominating at low temperature and pressures, and B - Ta_2O_5 stabilized under high-temperature and high-pressure conditions. The precisely clarified stability ranges of γ - Ta_2O_5 and B - Ta_2O_5 , including their coexistence boundaries and metastable regimes, provide crucial theoretical guidance for targeted synthesis strategies, particularly for technological applications requiring structural robustness under ambient conditions versus extreme environments. Importantly, nuclear quantum effects (NQEs) are shown to significantly influence the phase stability sequence, highlighting their importance even in heavy-element systems such as transition metal oxides. The re-entrant phase transition between γ and B - Ta_2O_5 at $P \sim 2$ GPa is predicted, a demonstration of the nontrivial role of NQEs in the thermodynamics of this system. Another finding is the determination of characteristic temperature T_0 (approximately one-third of the Debye temperature), which physically corresponds to the crossover point where zero-point vibrations balance thermal phonon contributions to the free energy. Looking ahead, more advanced simulations that incorporate larger supercells and anharmonic effects, together with experimental validation, will be essential to further refine the stability map and assess the potential of wider range of applications.

Acknowledgements

This work is financially supported by the National Natural Science Foundation of China (No. 12074382, 11474285, 12464012). We are grateful to the staff of the Hefei Branch of Supercomputing Center of Chinese Academy of Sciences, and the Hefei Advanced Computing Center for support of supercomputing facilities. We would like to thank the crew of the Center for Computational Materials Science, Institute for Materials Research of Tohoku University, and the supercomputer resources through the HPCI System Research Project (hp200246). We also thank Yangwu Tong for

helpful discussions.

References:

- [1] A. K. Chu, Y. Y. Lu, and Y. Y. Lin, Fabrication and analysis of tantalum pentoxide optical waveguide resonator of high thermal stability, *Opt. Express* **27**, 6629 (2019).
- [2] K. F. Lamee, D. R. Carlson, Z. L. Newman, S. P. Yu, and S. B. Papp, Nanophotonic tantalum waveguides for supercontinuum generation pumped at 1560 nm, *Opt. Lett.* **45**, 4192 (2020).
- [3] S. G. Song *et al.*, Tantalum oxide and silicon oxide mixture coatings deposited using microwave plasma assisted co-sputtering for optical mirror coatings in gravitational wave detectors, *Appl. Opt.* **62**, B73 (2023).
- [4] L. F. Liu, L. Y. Pan, Z. G. Zhang, and J. Xu, Impact of Band-Engineering to Performance of High-k Multilayer Based Charge Trapping Memory, *Chin. Phys. Lett.* **32**, 088501 (2015).
- [5] S. Sun, L. Gao, P. Han, L. Zhu, W. M. Li, and A. D. Li, Atomic layer-deposited Ta_2O_5-x nano-islands for charge trapping memory devices, *Journal of Materials Chemistry C* **12**, 18676 (2024).
- [6] A. I. Kingon, J.-P. Maria, and S. K. Streiffer, Alternative dielectrics to silicon dioxide for memory and logic devices, *Nature* **406**, 1032 (2000).
- [7] J. M. M. Andrade, C. M. M. Rosário, S. Menzel, R. Waser, and N. A. Sobolev, Application of the Quantum-Point-Contact Formalism to Model the Filamentary Conduction in Ta_2O_5 -Based Resistive Switching Devices, *Phys. Rev. Appl.* **17**, 034062 (2022).
- [8] R. Waser, R. Dittmann, G. Staikov, and K. Szot, Redox-Based Resistive Switching Memories - Nanoionic Mechanisms, Prospects, and Challenges, *Adv. Mater.* **21**, 2632 (2009).
- [9] R. Wang, K. Chang, X. Zhao, X. Yu, S. Ma, Z. Zhao, and H. Wang, High-performance Ta_2O_5 -based resistive random-access memory with embedded graphene quantum dots and Pt–Ag composite active layer, *Appl. Phys. Lett.* **123** (2023).
- [10] J. Y. Kim, B. Magyari Köpe, K. J. Lee, H. S. Kim, S. H. Lee, and Y. Nishi, Electronic structure and stability of low symmetry Ta_2O_5 polymorphs, *Phys. Status Solidi RRL* **8**, 560 (2014).
- [11] A. M. Huerta-Flores *et al.*, Enhanced Photocatalytic Hydrogen Evolution from Water Splitting on $Ta_2O_5/SrZrO_3$ Heterostructures Decorated with $Cu_{(x)}O/RuO_{(2)}$ Cocatalysts, *ACS Appl. Mater. Interfaces* **14**, 31767 (2022).
- [12] R. Y. Li, Q. Q. Zhang, X. S. Li, N. N. Li, X. H. Liu, and Z. J. Li, Strongly coordinated synthesis of high-loading Ta_2O_5 -supported Ru–Fe–Ni single-atom electrocatalyst with enhanced catalytic performance for urea synthesis via multifunctional graphene quantum dot integration, *Journal of Electroanalytical Chemistry* **990**, 119163 (2025).
- [13] B. Osuagwu, W. Raza, A. B. Tesler, and P. Schmuki, A drastic improvement in photocatalytic H_2 production by TiO_2 nanosheets grown directly on Ta_2O_5 substrates,

Nanoscale **13**, 12750 (2021).

[14] E. Field, J. Bellum, and D. Kletecka, Laser damage comparisons of broad-bandwidth, high-reflection optical coatings containing TiO_2 , Nb_2O_5 , or Ta_2O_5 high-index layers, Opt. Eng. **56**, 011018 (2016).

[15] S. Pal *et al.*, Sol-gel prepared amorphous Ta_2O_5 thin film for application in high LIDT antireflection coating and UV photodetection, Opt. Mater. **142**, 114097 (2023).

[16] Y. Le, X. Ma, H. Xiao, C. Luan, B. Zhang, and J. Ma, High performance UV photodetectors based on W doped δ - Ta_2O_5 single crystalline films, Appl. Phys. Lett. **122** (2023).

[17] E. R. Singh, N. K. Almulhem, M. W. Alam, and N. K. Singh, UV photodetector based on vertically aligned Ta_2O_5 nanorods, Opt. Mater. **155**, 115858 (2024).

[18] C. Zhijun, Z. Keting, Y. Yongqiang, X. Pengwu, L. Ruiyi, W. Guangli, L. Zaijun, and L. Xiaohao, Ta_2O_5 -graphene Schottky heterojunction composite symmetric supercapacitor with ultrahigh energy density for self-powered pulse sensor driven by green long afterglow phosphor-enhanced solar cell, Appl. Surf. Sci. **605**, 154730 (2022).

[19] J. S. Santos, P. d. S. Araújo, Y. B. Pissolitto, P. P. Lopes, A. P. Simon, M. d. S. Sikora, and F. Trivinho-Strixino, The Use of Anodic Oxides in Practical and Sustainable Devices for Energy Conversion and Storage, Materials **14**, 383 (2021).

[20] P. Pohekar, B. B. Upadhyay, B. Parvez, S. Ganguly, and D. Saha, Introduction of charge-trapping $\text{Al}_2\text{O}_3/\text{Ta}_2\text{O}_5/\text{Al}_2\text{O}_3$ dielectric stack in AlGaN/GaN high electron mobility transistors for programmable threshold voltage, Appl. Phys. Lett. **126** (2025).

[21] N. Mohammadian, S. Faraji, S. Sagar, B. C. Das, M. L. Turner, and L. A. Majewski, One-Volt, Solution-Processed Organic Transistors with Self-Assembled Monolayer- Ta_2O_5 Gate Dielectrics, Materials **12**, 2563 (2019).

[22] S.-Y. Wong, M.-W. Liao, T.-K. Chin, and T.-P. Perng, Au nanoparticles loaded Ta_2O_5 @nanohoneycomb structure for visible-light-driven photocatalytic hydrogen evolution, Appl. Surf. Sci. **599**, 153620 (2022).

[23] W.-S. Liu, S.-H. Huang, C.-F. Liu, C.-W. Hu, T.-Y. Chen, and T.-P. Perng, Nitrogen doping in Ta_2O_5 and its implication for photocatalytic H₂ production, Appl. Surf. Sci. **459**, 477 (2018).

[24] C. C. Han and T. Wang, Tantalum Pentoxide: From Crystal Structures to Applications in Water Splitting, Energy Fuels **37**, 13624 (2023).

[25] M. Chen, Z. Yi, Y. Bu, Q. Zhang, D. Gan, J. Qiu, E. Zhang, and J. Hu, Enhanced antibacterial and osteogenic properties of titanium by sputtering a nanostructured fluoride-doped tantalum oxide coating, Appl. Surf. Sci. Adv. **668**, 160393 (2024).

[26] V. K. Dommeti, S. Roy, S. Pramanik, A. Merdji, A. Ouldyerou, and M. Özcan, Design and Development of Tantalum and Strontium Ion Doped Hydroxyapatite Composite Coating on Titanium Substrate: Structural and Human Osteoblast-like Cell Viability Studies, Materials **16**, 1499 (2023).

[27] M. Zhang, Y. Xue, X. Huang, D. Ma, J. Gao, S. Yu, L. Zhu, and Y. Wu, Cytocompatibility and osteogenic activity of Ta-Ti-O nanotubes anodically grown on $\text{Ti}_6\text{Al}_4\text{V}$ alloy, Appl. Surf. Sci. **614**, 156165 (2023).

[28] S. Lagergren and A. Magnéli, On the Tantalum - Oxygen System, Acta Chem.

Scand. **6**, 444 (1952).

[29] K. Lehovec, Lattice structure of β -Ta₂O₅, Journal of the Less Common Metals **7**, 397 (1964).

[30] L. D. Calvert and P. H. G. Draper, A PROPOSED STRUCTURE FOR ANNEALED ANODIC OXIDE FILMS OF TANTALUM, Canadian Journal of Chemistry **40**, 1943 (1962).

[31] N. C. Stephenson and R. S. Roth, Structural systematics in the binary system Ta₂O₅–WO₃. V. The structure of the low-temperature form of tantalum oxide L-Ta₂O₅, Acta Crystallogr. Sect. B **27**, 1037 (1971).

[32] L. A. Aleshina and S. V. Loginova, Rietveld analysis of X-ray diffraction pattern from β -Ta₂O₅ oxide, Crystallogr. Rep. **47**, 415 (2002).

[33] R. Ramprasad, First principles study of oxygen vacancy defects in tantalum pentoxide, Journal of Applied Physics **94**, 5609 (2003).

[34] I. P. Zibrov, V. P. Filonenko, M. Sundberg, and P.-E. Werner, Structures and phase transitions of B-Ta₂O₅ and Z-Ta₂O₅: two high-pressure forms of Ta₂O₅, Acta Crystallogr. B **56**, 659 (2000).

[35] H. Fujikawa and Y. Taga, Effects of additive elements on electrical properties of tantalum oxide films, Journal of Applied Physics **75**, 2538 (1994).

[36] H. U. Hummel, R. Fackler, and P. Remmert, Tantaloxide durch Gasphasenhydrolyse, Druckhydrolyse und Transportreaktion aus 2H-TaS₂: Synthesen von TT-Ta₂O₅ und T-Ta₂O₅ und Kristallstruktur von T-Ta₂O₅, Ber. **125**, 551 (1992).

[37] A. Fukumoto and K. Miwa, Prediction of hexagonal Ta₂O₅ structure by first-principles calculations, Physical Review B **55**, 11155 (1997).

[38] S.-H. Lee, J. Kim, S.-J. Kim, S. Kim, and G.-S. Park, Hidden Structural Order in Orthorhombic Ta₂O₅, Phys. Rev. Lett. **110**, 235502 (2013).

[39] S. Pérez-Walton, C. Valencia-Balvín, A. C. M. Padilha, G. M. Dalpian, and J. M. Osorio-Guillén, A search for the ground state structure and the phase stability of tantalum pentoxide, Journal of Physics-Condensed Matter **28**, 035801 (2016).

[40] Y. Yang and Y. Kawazoe, Prediction of new ground-state crystal structure of Ta₂O₅, Phys. Rev. Mater. **2**, 034602 (2018).

[41] A. Pedrielli, N. M. Pugno, M. Dapor, and S. Taioli, In search of the ground-state crystal structure of Ta₂O₅ from ab initio and Monte Carlo simulations, Computational Materials Science **216**, 111828 (2023).

[42] J.-H. Yuan, K.-H. Xue, Q. Chen, L. R. C. Fonseca, and X.-S. Miao, Ab Initio Simulation of Ta₂O₅: A High Symmetry Ground State Phase with Application to Interface Calculation, Ann. Phys. **531**, 1800524 (2019).

[43] Y. W. Tong, H. M. Tang, and Y. Yang, Structural and electronic properties of Ta₂O₅ with one formula unit, Computational Materials Science **230**, 112482 (2023).

[44] M. C. Brennan, D. A. Rehn, L. Q. Huston, and B. T. Sturtevant, Phase comparison and equation of state for Ta₂O₅, Journal of Physics-Condensed Matter **36**, 275401 (2024).

[45] Q. Li *et al.*, Pressure-induced amorphization in orthorhombic Ta₂O₅: An intrinsic character of crystal, Journal of Applied Physics **115**, 193512 (2014).

[46] E. Stavrou, J. M. Zaug, S. Bastea, and M. Kunz, A study of tantalum pentoxide

Ta₂O₅ structures up to 28 GPa, *Journal of Applied Physics* **121**, 175901 (2017).

[47] M. C. Brennan, S. C. Vogel, and B. T. Sturtevant, Crystal structure and thermal expansion of Ta₂O₅ from neutron diffraction, *Phys. Rev. Materials* **9**, 073605 (2025).

[48] Y. Gong, H. Tang, Y. Yang, and Y. Kawazoe, Possible Orthorhombic Phase of Ta₂O₅ under High Pressures, *Chinese Physics B* **34**, 116104 (2025).

[49] M. A. Morales, J. M. McMahon, C. Pierleoni, and D. M. Ceperley, Nuclear Quantum Effects and Nonlocal Exchange-Correlation Functionals Applied to Liquid Hydrogen at High Pressure, *Phys. Rev. Lett.* **110**, 065702 (2013).

[50] Y. Litman, D. Donadio, M. Ceriotti, and M. Rossi, Decisive role of nuclear quantum effects on surface mediated water dissociation at finite temperature, *J. Chem. Phys.* **148**, 102320 (2018).

[51] X. Z. Meng, J. Guo, J. B. Peng, J. Chen, Z. C. Wang, J. R. Shi, X. Z. Li, E. G. Wang, and Y. Jiang, Direct visualization of concerted proton tunnelling in a water nanocluster, *Nat. Phys.* **11**, 235 (2015).

[52] J. Guo *et al.*, Nuclear quantum effects of hydrogen bonds probed by tip-enhanced inelastic electron tunneling, *Science* **352**, 321 (2016).

[53] C. Andreani, D. Colognesi, A. Pietropaolo, and R. Senesi, Ground state proton dynamics in stable phases of water, *Chem. Phys. Lett.* **518**, 1 (2011).

[54] Y. Yang and Y. Kawazoe, Adsorption and Diffusion of H Atoms on β -PtO₂ Surface: The Role of Nuclear Quantum Effects, *J. Phys. Chem. C* **123**, 13804 (2019).

[55] C. Bi, Q. Chen, W. Li, and Y. Yang, Quantum nature of proton transferring across one-dimensional potential fields, *Chin. Phys. B* **30**, 046601 (2021).

[56] Y. W. Tong and Y. Yang, Hydrogen Diffusion on Graphene Surface: The Effects of Neighboring Adsorbate and Quantum Tunneling, *J. Phys. Chem. C* **128**, 840 (2024).

[57] G. Kresse and J. Furthmüller, Efficient iterative schemes for ab initio total-energy calculations using a plane-wave basis set, *Phys. Rev. B Condens. Matter* **54**, 11169 (1996).

[58] G. Kresse and J. Hafner, Ab initio molecular dynamics for liquid metals, *Phys. Rev. B* **47**, 558 (1993).

[59] G. Kresse and D. Joubert, From ultrasoft pseudopotentials to the projector augmented-wave method, *Phys. Rev. B* **59**, 1758 (1999).

[60] P. E. Blöchl, Projector augmented-wave method, *Phys. Rev. B* **50**, 17953 (1994).

[61] J. P. Perdew, K. Burke, and M. Ernzerhof, Generalized Gradient Approximation Made Simple, *Phys. Rev. Lett.* **77**, 3865 (1996).

[62] A. Togo, F. Oba, and I. Tanaka, First-principles calculations of the ferroelastic transition between rutile-type and CaCl₂-type SiO₂ at high pressures, *Phys. Rev. B* **78**, 134106 (2008).

[63] L. Chaput, A. Togo, I. Tanaka, and G. Hug, Phonon-phonon interactions in transition metals, *Phys. Rev. B* **84**, 094302 (2011).

[64] A. Togo and I. Tanaka, First principles phonon calculations in materials science, *Scripta Materialia* **108**, 1 (2015).

[65] S. Baroni, S. de Gironcoli, A. Dal Corso, and P. Giannozzi, Phonons and related crystal properties from density-functional perturbation theory, *Reviews of Modern*

Physics **73**, 515 (2001).

[66] R. Wang, S. Wang, X. Wu, M. Lan, and T. Song, First-principles calculations of phonon and thermodynamic properties of AlRE (RE= Y, Gd, Pr, Yb) intermetallic compounds, *Physica Scripta - PHYS SCR* **85** (2012).

[67] H. J. Monkhorst and J. D. Pack, Special points for Brillouin-zone integrations, *Phys. Rev. B* **13**, 5188 (1976).

[68] Y. Yang, H. H. Nahm, O. Sugino, and T. Ohno, Electronic structures of oxygen-deficient Ta₂O₅, *AIP Adv.* **3**, 042101 (2013).

[69] P. Zhang, B.-T. Wang, and X.-G. Zhao, Ground-state properties and high-pressure behavior of plutonium dioxide: Density functional theory calculations, *Phys. Rev. B* **82**, 144110 (2010).

[70] T. Hamada and K. Takenaka, Phase instability of magnetic ground state in antiperovskite Mn₃ZnN: Giant magnetovolume effects related to magnetic structure, *J. Appl. Phys.* **111** (2012).

[71] H. Qin, S.-H. Zhu, Z. Jiao, F.-S. Liu, Z.-T. Liu, and Q.-J. Liu, A simulation study on the phase transition behavior of solid nitrogen under extreme conditions, *Phys. Chem. Chem. Phys.* **25**, 11653 (2023).

[72] D. Laniel *et al.*, A reentrant phase transition and a novel polymorph revealed in high-pressure investigations of CF₄ up to 46.5 GPa, *J. Chem. Phys.* **156** (2022).

[73] T. Matsuoka *et al.*, Pressure-induced reentrant metallic phase in lithium, *Physical Review B* **89**, 144103 (2014).

[74] Y.-H. Na, Y. Naruse, N. Fukuda, H. Orihara, A. Fajar, V. Hamplova, M. Kaspar, and M. Glogarova, E-T Phase Diagrams of an Antiferroelectric Liquid Crystal with Re-Entrant Smectic C* Phase, *Ferroelectrics* **364**, 13 (2008).

[75] L. Radzihovsky, Entropically driven re-entrant SmC-SmA-SmC phase transition in composite polymer–liquid-crystal systems, *Europhysics Letters* **36**, 595 (1996).

[76] Y. Yang and Y. Kawazoe, Characterization of zero-point vibration in one-component crystals, *Europhys. Lett.* **98**, 66007 (2012).